Macromolecules **2000,** *33,* 9747−9756

Combinatorial Materials Science for Polymer Thin-Film Dewetting

J. Carson Meredith,[†] Archie P. Smith, Alamgir Karim,* and Eric J. Amis

Polymers Division, National Institute of Standards and Technology, 100 Bureau Dr. Stop 8542, Gaithersburg, Maryland 20899-8542

Received July 25, 2000

ABSTRACT: Combinatorial methods involving data collection in multiparameter space allow a rapid identification of measured property trends as a function of system parameters. The technique has been applied with success to pharmaceutical, inorganic and organic materials synthesis, but not significantly to measurements of polymeric films and coatings. We demonstrate the use of 2-D combinatorial libraries to investigate thin-film dewetting. We have prepared libraries of thin films of polystyrene on silicon substrates containing orthogonal, continuous variations of thickness (h), and temperature (T) that represent about 1200 practical state points per library. The libraries were screened for dewetting behavior using automated optical microscopy. Dewetting trends were visibly apparent on the libraries, and a comprehensive map of the T, h, and time (t) dependence was generated in a few hours. The combinatorial libraries, spanning a large T, h, and t range, not only reproduced known dewetting structures and phenomena but also enabled a novel T, h superposition of the heterogeneous nucleated hole dewetting kinetics. We observed three hole nucleation regimes as a function of thickness: heterogeneously nucleated holes ($h > 55$ nm), a crossover regime where both heterogeneous and capillary instability nucleation compete (33 nm $< h <$ 55 nm), and a regime of holes nucleated by capillary instability (16 nm $< h <$ 33 nm).

Introduction

Combinatorial and high-throughput characterization methods have changed the paradigm of pharmaceutical research and are likely to have a similar impact on materials science.[1−3] Already there are examples of combinatorial methods for inorganic[4−11] and organic[12−17] materials synthesis. In the midst of the excitement to "make things" with high-throughput synthesis methods, another opportunity arises to make measurements and "understand things" with combinatorial methods. Rapid and systematic generation of experimental data in multiparameter space using combinatorial methods can facilitate the observation of novel phenomena and the development of predictive models. Combinatorial methods also can be used as a primary screen of parameter space to identify regimes of interest for traditional one-sample-for-one-measurement investigations.

This paper reports the use of two-dimensional combinatorial libraries to characterize materials properties of polymeric thin films. In a recent paper, we reported combinatorial methods for mapping thin film polymer blend phase behavior.[18] We applied standard concepts of combinatorial methods: library creation, high-throughput assays, and informatics to investigate phase separation. In this work we extend the methodology to the physics of polymer thin film dewetting behavior. Dewetting represents an ideal phenomenon for combinatorial analysis because a number of parameters interact to create complex thermodynamic and kinetic behavior. In addition, polymer thin-film dewetting is fundamental to technologies including microelectronics, lubricants, adhesives, and coatings. The critical variables that determine film stability and dewetting kinetics are thickness (h), molecular mass (M_r), surface chemistry, and temperature (T).[19−21] The breadth of parameter space and the complex interactions among these variables present a significant challenge to conventional experimental methodologies, so that previous studies usually varied only single parameters (e.g, h, M_r). In particular, systematic studies of the effect of T on dewetting kinetics have not been reported.

Unfortunately, many of the vapor phase and high-temperature techniques (e.g., sputtering) used to deposit libraries of inorganic materials are not applicable to polymers. In the Experimental Methodology we present novel methods for creating continuous and orthogonal gradients in T and h for polymer thin films. Automated optical microscopy is used for high-throughput screening of the T, h libraries to identify wetted versus dewetted regions and to measure the T and h dependence of dewetted structure type, size, density, and evolution rate. We demonstrate that combinatorial libraries reproduce dewetted structures observed in previous noncombinatorial studies.[20,22−24] We then present several novel observations of the temperature dependence of dewetting kinetics and thickness dependence of nucleation, made possible by screening a large variable space with combinatorial methods.

Experimental Methodology

Library Creation. Figure 1 gives a schematic description of the application of the combinatorial method to thin-film dewetting. We prepared film libraries in which temperature (T) and thickness (h) were varied systematically over the substrate, sampling multiple processing conditions and film properties simultaneously. Thickness gradients were prepared on "piranha-etched"[25,26] silicon wafers (Polishing Corporation of America)[27] with a velocity-gradient, knife-edge coating apparatus. A drop of polymer solution was spread over the substrate under an angled steel blade (5° relative to substrate) at constant acceleration by using a feedback-controlled translation stage (Compumotor). The solvent dried within seconds of spreading and resulted in a polymer film with a gradient in thickness. Solutions

---

[†] Present address: School of Chemical Engineering, Georgia Institute of Technology, Atlanta, GA 30332-0100.

10.1021/ma001298g CCC: $19.00

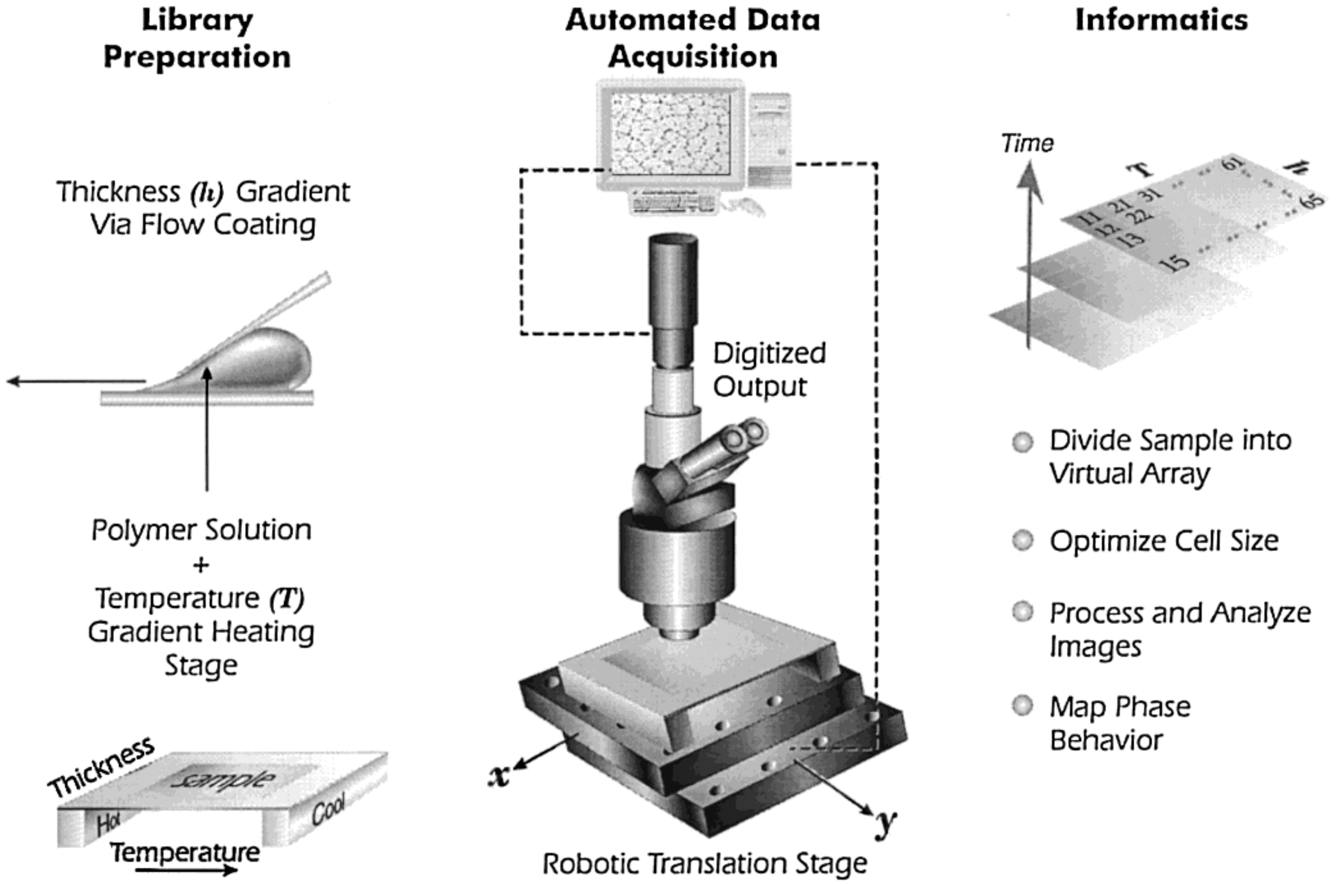

Figure 1. Schematic representation of the three steps involved in combinatorial measurements of polymer thin films: (1) preparation of thickness and temperature gradient libraries, (2) automated optical microscopy, and (3) informatic data reduction. Illustration by Jeffrey Aarons.

with mass fractions between 2% and 5% polystyrene (Goodyear, $M_r = 1900$, $M_r/M_n = 1.19$, where M_r and M_n are the mass- and number-average relative molecular masses) in toluene were used to prepare (25×35) mm^2 library samples with the thickness gradient in the short direction.

Thicknesses were measured using a UV−vis reflectance interferometer with a 0.5 mm diameter spot size (Filmetrics F20). Over the range 10−100 nm, reflectance measurements agreed with AFM control measurements to within 4%. Figure 2a presents representative thickness−gradient profiles and indicates how the range and shape of the profile are affected by solution composition. The initial and final thickness and the slope of the gradient can also be controlled by adjusting the blade−substrate gap width, substrate velocity, and acceleration. The gradients generally have power law or polynomial dependence on position, x (mm), on the wafer, depending on the flow conditions. Modeling the gradient profile shape as a function of flow parameters is beyond the scope of this paper; however, the frictional drag of the solution against the blade increases with velocity and limits the amount of solution that can pass through the gap and form the final film.[28] The velocity dependence of the blade−substrate drag, as well as the solution surface tension, determines the shape of the film thickness gradient.

Experiments were repeated and confirmed with eight combinatorial libraries. We present detailed representative results from two libraries covering distinct but overlapping thickness regimes. For detailed results presented here, library A ranges in thickness from 16 to 33 nm according to $h = 16.0 + 2.15x - 0.125x^2 + 0.00298x^3$ $(0 < x < 20)$ mm, and library B extends the thickness range from 33 to 90 nm with $h = 33.1x^{0.30}$ $(1 < x < 28)$ mm. The standard deviation in measured h values relative to these fitted curves was ±1.5 nm.

To initiate the dewetting, the thin film was exposed to a continuous temperature gradient, *orthogonal* to the thickness gradient, by placing the wafer with the thickness gradient film on an aluminum heating stage (Figure 1). This T-gradient stage employs a heat source and a heat sink that results in a linear gradient ranging between adjustable end-point temperatures. The end-point temperatures used for this study were 135.0 ± 0.5 to 75.0 ± 0.1 °C over 40 mm, yielding a gradient of 2 °C/mm. Surface temperature measurements verified the linearity of the T-gradient. The T-gradient stage is sealed with an O-ring surrounding the sample wafer and glass plate over it to maintain a vacuum of 1 bar. This precaution minimizes sample oxidation and convective heat transfer from the substrate surface. Taking $\Delta T = 0.5$ °C and $\Delta h = 3$ nm as defining a practical "state point," each combinatorial library contained about 1200 state points in T and h. One can verify that the relatively weak thickness and temperature gradients do not induce appreciable flow in the polymer film over the experimental time scale. Modeling the film with unidirectional Navier−Stokes equations for flow over a flat plate, the film is estimated to flow at a characteristic velocity of 1 μm/h at $T = 135$ °C in response to the thickness gradient.[28] This small flow is orders of magnitude slower than the *dewetting* velocities on our libraries (as we will demonstrate) and changes the

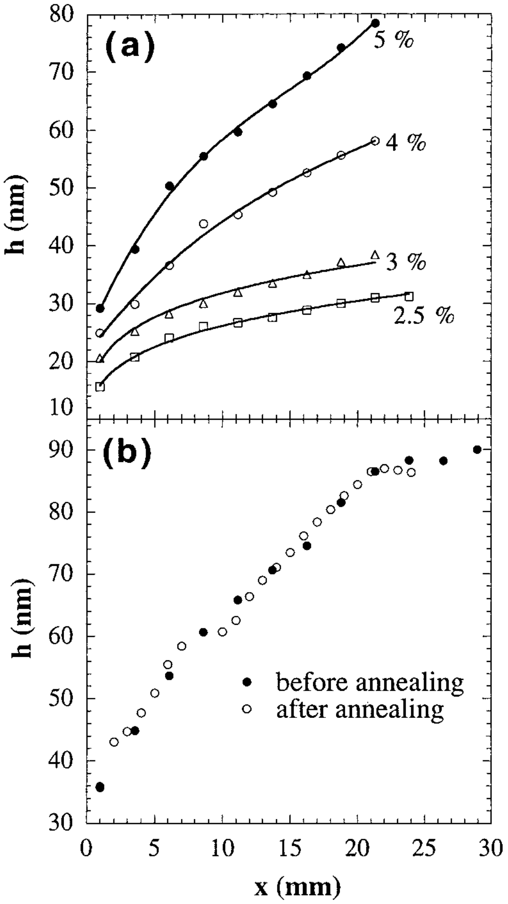

Figure 2. (a) Thickness gradient profiles as measured by ellipsometry for PS mass fraction 2−5% in toluene. The velocity-gradient flow-coating parameters were blade−substrate gap = 300 μm, maximum velocity = 9 mm/s, and acceleration = 1.5 mm/s^2. (b) Thickness gradient profiles before and after annealing on the temperature gradient stage for a film flow coated from a mass fraction 5% PS solution using the same parameters as in (a). The temperature gradient was 135−85 °C over 30 mm. The two profiles agree well, indicating that the film does not flow appreciably during the annealing process. The thickness measurement after heating was based on areas that did not significantly dewet during the annealing time of 2 h.

initial thickness only by about 0.5 nm/h in each image area. To check for gravitational or convection flow, we examined four thickness-gradient libraries before and after heating on the temperature gradient stage. Based on T regions that did not significantly dewet within the annealing time of 2 h, the difference of thickness gradients before and after annealing was within the standard uncertainty of ±1.5 nm, shown in Figure 2b.

High-Throughput Screening. An automated optical microscope (Nikon Optiphot 2) was used to monitor the evolution of dewetted microstructures on the libraries. A black and white CCD camera (Kodak ES1.0) coupled to the microscope sent 1024 × 1024 pixel, 8 bit digitized images to a computer that also synchronized sample stage movement over a grid of T and h conditions using motorized translation stages. At the beginning of each time cycle, the translation stage returned to a home position to within ±0.5 μm. In a typical experiment, the $T-h-t$ dependence of dewetting structures was followed by collecting a 5 by 5 array of 200× or 500× magnification images every 5 min over a period of 2 h, for a total of 600 images. Thus, each image represents the dewetting at a certain point in $T-h-t$ space. At the completion of the experiment a 5 by 6 array of lower magnification images is collected and used to create a mosaic image of the entire library (Figure 3).

Because of a concern that the two-dimensional gradients in thickness and temperature might distort the evolution of dewetted structures, control experiments were performed on one-dimensional gradient samples, in addition to our comparison to literature results from uniform samples. We performed spot-checks for certain T and h values with constant thickness samples heated on the temperature gradient stage and constant temperature samples that contained thickness gradients. The dewetted structures that occurred on one-dimensional controls and two-dimensional libraries were identical, within experimental uncertainty, for the same wafer preparation conditions.

Informatic Analysis. For quantitative analysis of images, we averaged the library T and h values over an arbitrary image area and indicate these average values as $\bar{T}$ and $\bar{h}$. The library data are thus divided into a virtual array of images that each correspond to a particular $\bar{T}$, $\bar{h}$, and t. By using a custom batch program (NIH Image), optical images are automatically thresholded, and the dewetted area fraction, A_d, is measured based upon the inner dewet hole area (excluding hole rims). Using a larger image area for analysis increases the number of structures observed at each $\bar{T}$, $\bar{h}$, and t, which improves the statistics of hole size measurement leading to more representative results. On the other hand, larger images also increase the variance in $\bar{T}$ and $\bar{h}$ over the image area because of the gradients. The proper selection of image size for analysis must reflect a balance between counting statistics and variance in $\bar{T}$ and $\bar{h}$, e.g., $\Delta\bar{T}$ and $\Delta\bar{h}$. For library A, a 500× image contains over 100 holes with a standard uncertainty along each cell edge of $\Delta\bar{T} = 0.4$ °C and $\Delta\bar{h} = 3.0$ nm, respectively. Since the structures on library B are larger, a 200× image is used, which yields standard uncertainties of $\Delta\bar{T} = 1.0$ °C and $\Delta\bar{h} = 6.0$ nm. Based on these variances, libraries A and B contain approximately 2450 unique $\bar{T}$, $\bar{h}$ conditions. It would take at least several months to screen dewetting behavior for 2450 individual conditions by traditional methods, but with combinatorial methods these $\bar{T}$, $\bar{h}$ conditions can be screened in a few hours per library.

Results

Figure 3 presents a composite set of optical microscope images of library B at $t = 2$ h. (Structures on library A are too small to be represented at the print resolution of Figure 3, and higher magnification images from library A are presented instead in Figure 4.) The overall wetted and dewetted pattern features are in fact visible as dark and bright regions, respectively, to the unaided eye. Figure 4 shows selected regions from wafers A and B with higher magnification optical and atomic force microscopy (AFM, Digital Instruments Dimension 3000). There are several distinct regions with different dewetted structures and kinetics. For $\bar{h} >$ 57 nm, discrete circular holes in the film nucleate and grow at a rate dependent on $\bar{T}$ (quantification of the rate is given in Figure 6). In this thickness regime is a demarcation in $\bar{T}$ and $\bar{h}$ space separating low $\bar{T}$, slow-growing isolated holes (Figure 4d) from high $\bar{T}$, fast growing holes (Figure 4a) that have impinged to form polygons. Higher magnification reveals particles in the

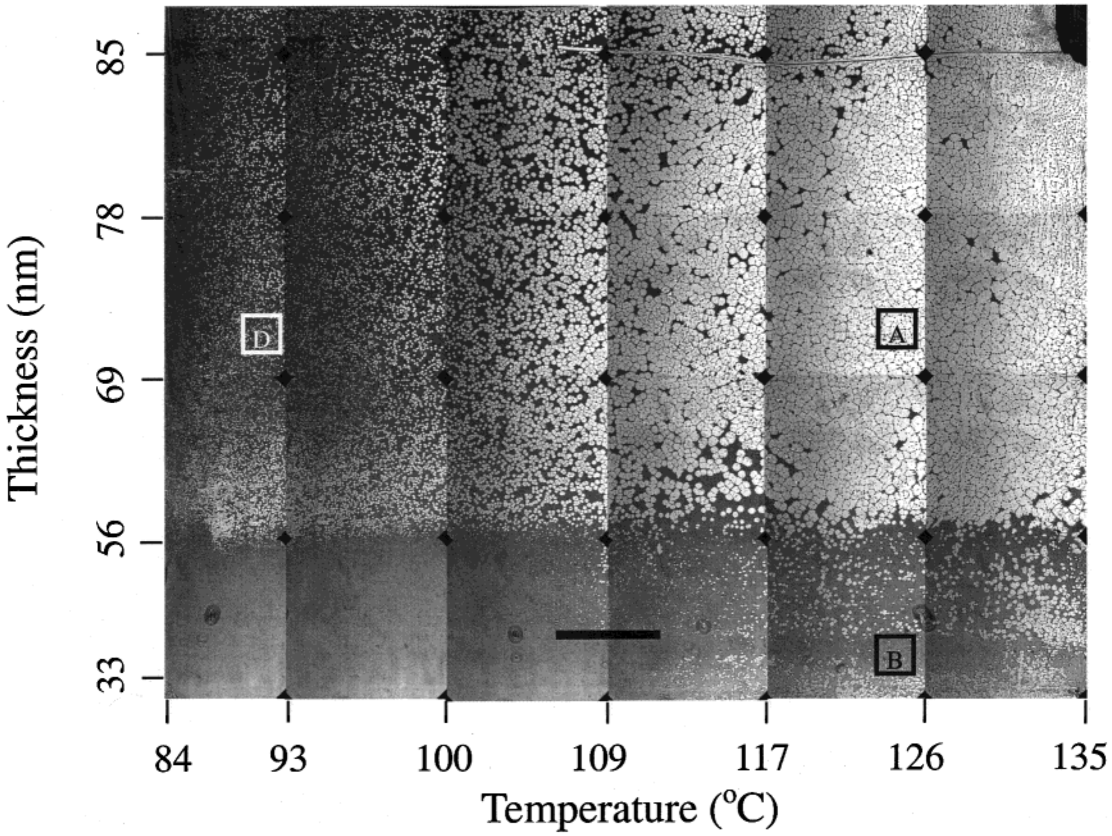

Figure 3. Composite of optical images of library B combinatorial library of PS on silicon, $t = 2$ h, 25× magnification. Boxed regions A, B, and D identify higher magnification images given in Figure 4a,b,d. Scale bar = 2.0 ± 0.1 mm. The thickness scale is a power law function, reflecting the nonlinear thickness gradient deposition procedure. Images from library A are too small to be reasonable represented at the scale used in Figure 3.

centers of many of the holes that may indicate heterogeneous nucleation sites for $\bar{h} > 57$ nm. AFM images indicate that the *unbroken* film surface (Figure 5a) is smooth for $\bar{h} > 57$ nm, with a root-mean-square (rms) roughness of 1 nm and no periodic structure.

Below $\bar{h} \approx 57$ nm, there is a sharp and temperature-independent transition to a regime where irregular, asymmetrical holes (Figure 4b) nucleate and grow more slowly than at higher thicknesses. Figure 4e shows an optical micrograph from a region similar to Figure 4b, at higher magnification. The thresholded image indicates two patterns: asymmetrical holes surrounded by bicontinuous undulations in the film surface. The bicontinuous undulations do not break the surface of the film after 2 h. A similar structure consisting of asymmetrical holes that break up into a bicontinuous pattern at late stage, termed an "intermediate morphology", has been observed recently for 12 nm thick films of poly(styrene-*ran*-acrylonitrile).[29] As measured by AFM (Figure 5b), the film surface below $h = 57$ nm is roughened with correlated surface undulations. For example, Figure 5b shows an AFM image for $\bar{h} = 36$ nm with rms roughness of 6.5 nm, compared to the 1 nm roughness of the unbroken surface for $\bar{h} > 57$ nm. The 2D Fourier transform (Figure 5b) shows a strong correlation peak, and the undulations have an average spacing of $1/q_{\max} = 7\ \mu$m. The onset thickness, below which asymmetrical holes and correlated undulations are observed (57 nm in Figure 3), is measured to be 55 ± 4 nm from *five different* combinatorial libraries. The deviation in this onset thickness is presumed to be caused by small differences in the silicon oxide layer introduced during substrate cleaning.

Below $\bar{h} \approx 33$ nm, another transition in structure is apparent from higher magnification images of library A. For these thicknesses, holes (Figure 4f) grow more quickly than in the region 33 nm < $\bar{h}$ < 57 nm and impinge to form small polygons (Figure 4c) within several minutes to about 2 h, depending on $\bar{T}$. By collecting the comprehensive $\bar{T}$, $\bar{h}$, and t dependence of dewetting, these trends in the structures are immediately observed and serve as a guide for detailed study of each regime, model selection, and quantitative analysis.

We note that there are a few small patches on the libraries (Figure 3) that have wetted or dewetted areas that are discontinuous from the surrounding areas. These spurious areas, which amount to less than 5% of the surface area, probably represent nonequilibrium regions or chemical heterogeneities introduced during wafer preparation, a complication inherent to all (even noncombinatorial) thin-film studies. The results of this paper do not depend on these spurious regions, and they can be excluded from the analysis that follows.

We performed a quantitative analysis of the thickness and temperature dependence of dewetted structures on the sample libraries as a function of thickness. Figure 6a shows the number density, N_p (N_h), and circular effective diameter, D_p (D_h), of polygons (holes) at $\bar{T} = 124$ °C and $t = 2$ h over the entire thickness range. Three regimes are observed: $\bar{h} < 33$ nm, 33 nm < $\bar{h}$ < 57 nm, and $\bar{h} > 57$ nm. Linear least-squares fits to the data for $\bar{h} < 33$ nm indicate that $N_p \sim \bar{h}^{-4.3\pm0.3}$ and $D_p \sim \bar{h}^{-2.1\pm0.1}$. These scaling exponents were also observed in previous work with uniform samples[20,22] and are predicted from theory[21,32] for nucleation by capillary

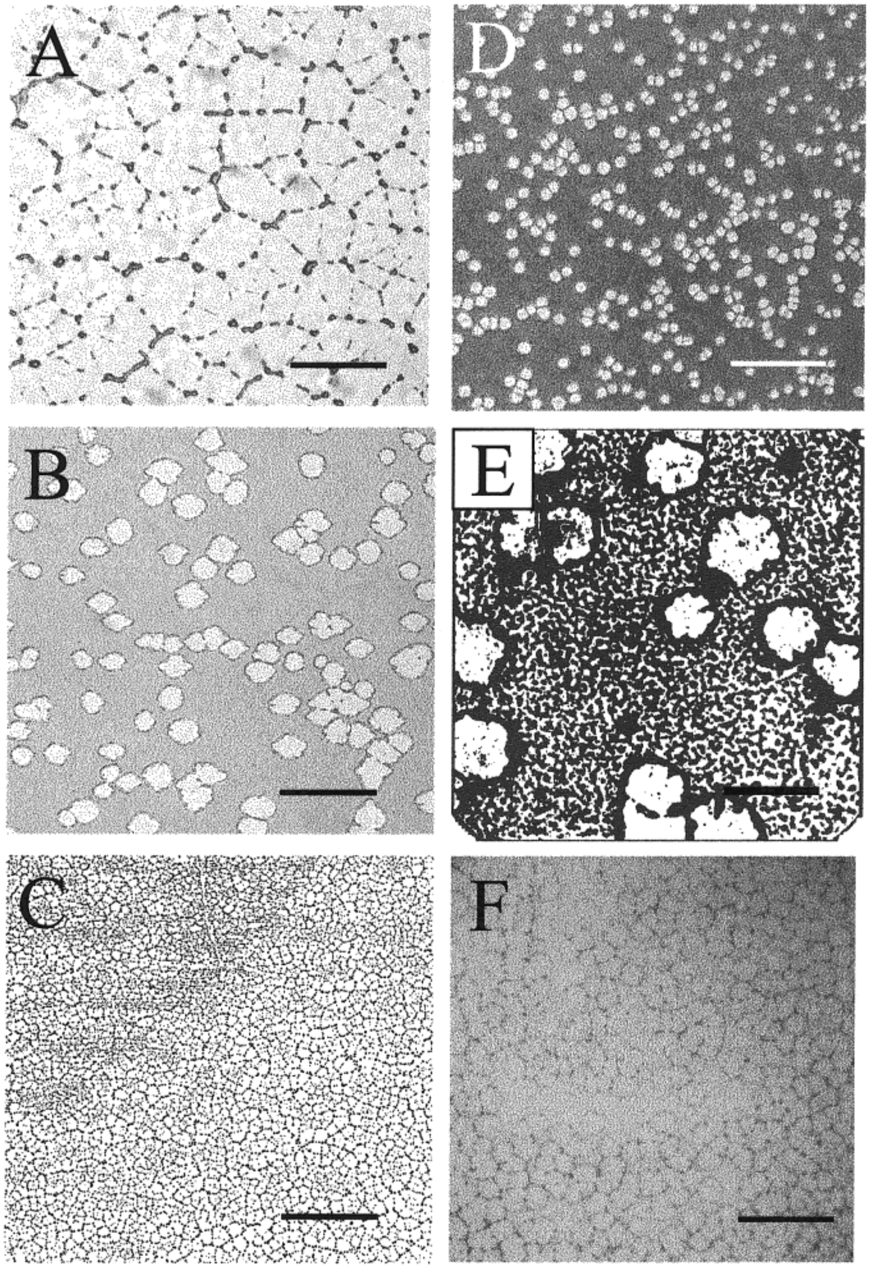

Figure 4. Close-up optical images of boxed regions from Figure 2, specified by [$\bar{T}$ °C, $\bar{h}$ nm], illustrating the variety of structures observed on the combinatorial libraries. (A) [124, 71], polygons typical for $h > 57$ nm; (B) [124, 36], asymmetrical holes typical of $33 < h < 57$ nm; (C) [128, 24], small polygons typical of $h < 33$ nm; (D) [92, 71], symmetrical holes; (E) [124, 36], high-magnification thresholded image typical of regime $33 < h < 57$ nm (as in (b)) indicating two patterns: asymmetrical holes and bicontinuous undulations; (F) [123, 31], high-magnification image of early stage of dewetting typical of $h < 33$ nm. Scale bar = 640 ± 10 μm for (A)−(D), 55 ± 5 μm for (E), and 64 ± 2 μm for (F).

instability. For $\bar{h} > 57$ nm, N_p and D_p are essentially invariant with $\bar{h}$, indicating randomly dispersed nucleation sites. The intermediate regime, 33 nm $< \bar{h} <$ 57 nm, shown by the shaded region in Figure 6a, indicates a crossover for the nucleation and structure size dependence on $\bar{h}$, an issue expanded upon in the discussion. Based on the dewetted area versus time profiles (Figure 6b), dewetting approaches late stage within 2 h at 124 °C for $\bar{h} < 33$ nm and $\bar{h} > 57$ nm. However, it is important to note that the regime $33 < \bar{h} < 57$ nm is not at late stage "equilibrium" after 2 h of annealing at 124 °C. The holes in this crossover or intermediate regime grow slower (rate given in Figure 6c), and the structures are qualitatively different (i.e., asymmetrical holes and surface undulations) than for $\bar{h} < 33$ nm and $\bar{h} > 57$ nm. The plateau in D_h in the shaded region of Figure 6a is caused by the fact that the slowly growing asymmetrical holes in the crossover regime have not yet reached late stage. In the discussion these differences in morphology and dewetting rate are described in terms of heterogeneous versus capillary instability hole nucleation and growth.

Systematic studies of the temperature dependence of dewetting rates have not been reported to our knowledge. However, through its effect on viscosity, T has a strong influence on hole drainage rates. The T-gradient libraries presented here offer a convenient means to assay a broad range of temperatures and dewetting rates in a single experiment. The inset to Figure 6b shows the raw dewetted area fraction, A_d, versus t at

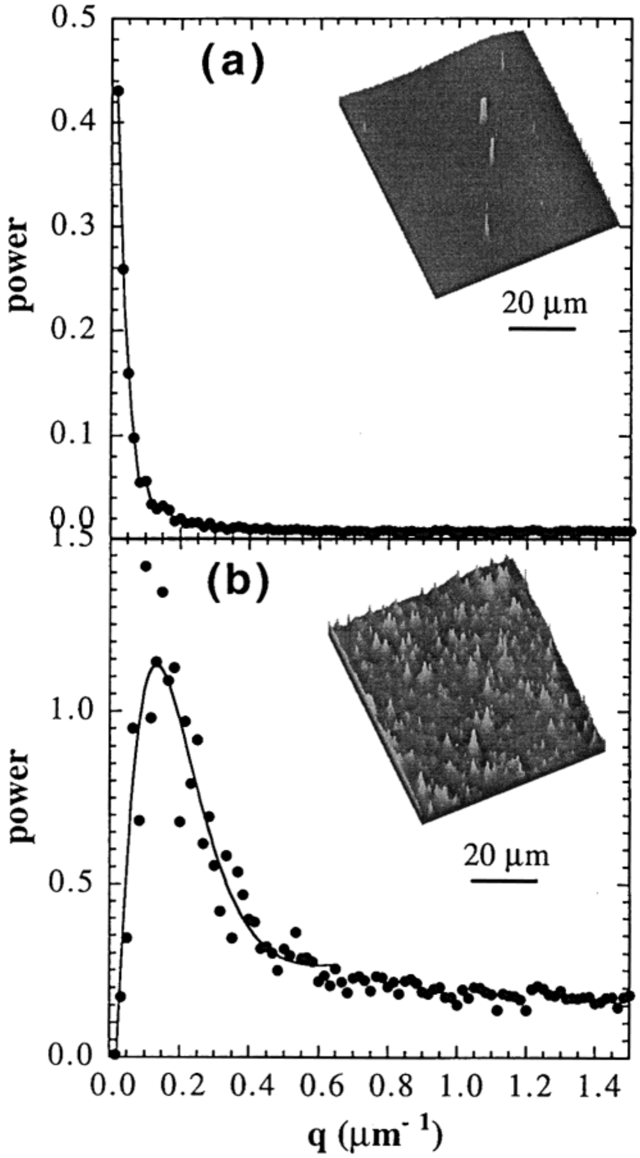

Figure 5. Radially averaged power spectrum of 2D Fourier transforms of AFM images (AFM images in inset) for film surfaces from library B at (a) $h = 71$ nm, typical of $h > 57$ nm, indicating a smooth surface and (b) $h = 36$ nm, typical of ($33 < h < 57$) nm, indicating a correlated spacing of $q_{\max} = 1.5\ \mu m^{-1}$, or $1/q_{\max} = 6.6\ \mu m$. The temperature region on library B where the images were taken was $T = 124 \pm 1$ °C.

various temperatures from library B for $\bar{h} = 79$ nm. Similar plots are obtained for each $\bar{h} > 57$ nm. The entire set of A_d vs t profiles for $\bar{h} > 57$ nm can be fitted with

$$A_d = A_{d\infty} + (A_{d0} - A_{d\infty}) \exp(-(t - t_0)/\tau) \qquad (1)$$

where A_{d0} and $A_{d\infty}$ are the dewet fractions at $t = t_0$ and $t = \infty$, τ is the dewetting time constant, and t_0 is a time delay for nucleation. As shown in Figure 6b, in reduced units of $(A_d - A_{d0})/(A_{d\infty} - A_{d0})$ versus $(t - t_0)/\tau$, the hole drainage profiles collapse onto the universal exponential curve given in eq 1. Figure 6b contains $\bar{T}$ and $\bar{h}$ data over a large range, $92 < \bar{T} < 135$ °C and $59 < \bar{h} < 86$ nm, and τ ranges from 2100 s (high temperatures) to 113 000 s (low temperatures). This universal behavior, which primarily reflects variations in the film viscosity (established later in the Discussion section), could be missed altogether by relying solely upon limited numbers of samples.

Figure 6c presents the dewetting velocities versus temperature from library B, for the early stage of hole drainage, calculated as the slope of the linear portion of A_d vs t, where holes are still isolated. For all thicknesses the velocity increases linearly with $\bar{T}$. For $\bar{h} = 71$, 79, and 86 nm, the velocities are independent of thickness at each temperature and have the same temperature dependence. However, the slope of v_A vs $\bar{T}$ is considerably smaller for thicknesses within the intermediate crossover regime of $33 < \bar{h} < 57$ nm, compared to $\bar{h} > 57$ nm. For example, at $\bar{h} = 33$ nm the velocities are about an order of magnitude lower than the dewetting velocities for $\bar{h} > 57$ nm. This difference between the drainage velocities in these two thickness regimes implies differences in hole growth mechanisms as a function of thickness, an issue discussed below.

Discussion

Interpreting Thickness Dependence. To interpret the dependence of hole and polygon density on thickness (Figure 6a) and the abrupt onset of an intermediate morphology (asymmetrical holes, correlated undulations, Figures 3–5) below 55 nm, we review briefly the factors influencing dewetting in our system. A nonwetting film is indicated by a negative spreading coefficient, $S = \gamma_{SO} - \gamma_{SL} - \gamma$, where γ_{SO}, γ_{SL}, and γ are the Si–air, Si–PS, and PS–air interfacial free energies, respectively.[19–21] Under these conditions, heterogeneities such as particles or voids[30] can nucleate randomly dispersed, symmetrical holes that grow and impinge upon one another to ultimately produce polygonal patterns. Sharma and Reiter report a value of $S = -8.1$ mJ/m^2 for the long-range (van der Waals) contributions that dominate molecular interactions in the Si/SiO$_x$/PS/air system.[26,31] Previous experimental studies have observed heterogeneous nucleation of holes for this same film–substrate system.[23,24,30]

Amplification of capillary fluctuations in the film surface is a second possible mechanism of film rupture in our system. Linearized capillary instability theory (LCIT)[21,32] predicts film instability when attractive long-range (i.e., van der Waals) interactions exist between the film and the substrate. Attractive long-range interactions are indicated by negative values of the effective Hamaker constant, A, where the dispersive film–substrate free energy of interaction is $G(h) = A/(12\pi h^2)$. Under these conditions capillary undulations greater than a critical wavelength are amplified by the negative disjoining pressure $(-\partial G/\partial h)$, leading to film rupture and spatially correlated dewetted structures. Table 1 presents effective A values from three previous studies of the Si/SiO$_x$/PS/air system that report evidence of capillary instability, using the definition of $G(h)$ given above. The difficulty in obtaining values of the substrate Hamaker constant can lead to a disparity in both the sign and magnitude in A, a subject discussed in detail elsewhere.[26,31,33] For example, the work reporting $A > 0$ in Table 1 appears to use typical metal oxide Hamaker constant values as an estimate for Si. The works reporting $A < 0$ calculate A by first relating it to S, a quantity available for a wider range of substrates. Despite challenges inherent to calculating A, extensive experimental evidence of capillary instability for the Si/SiO$_x$/PS/air system has been reported.[20,22–24,34]

However, for capillary instability to occur at an observable rate, the thickness must be less than an

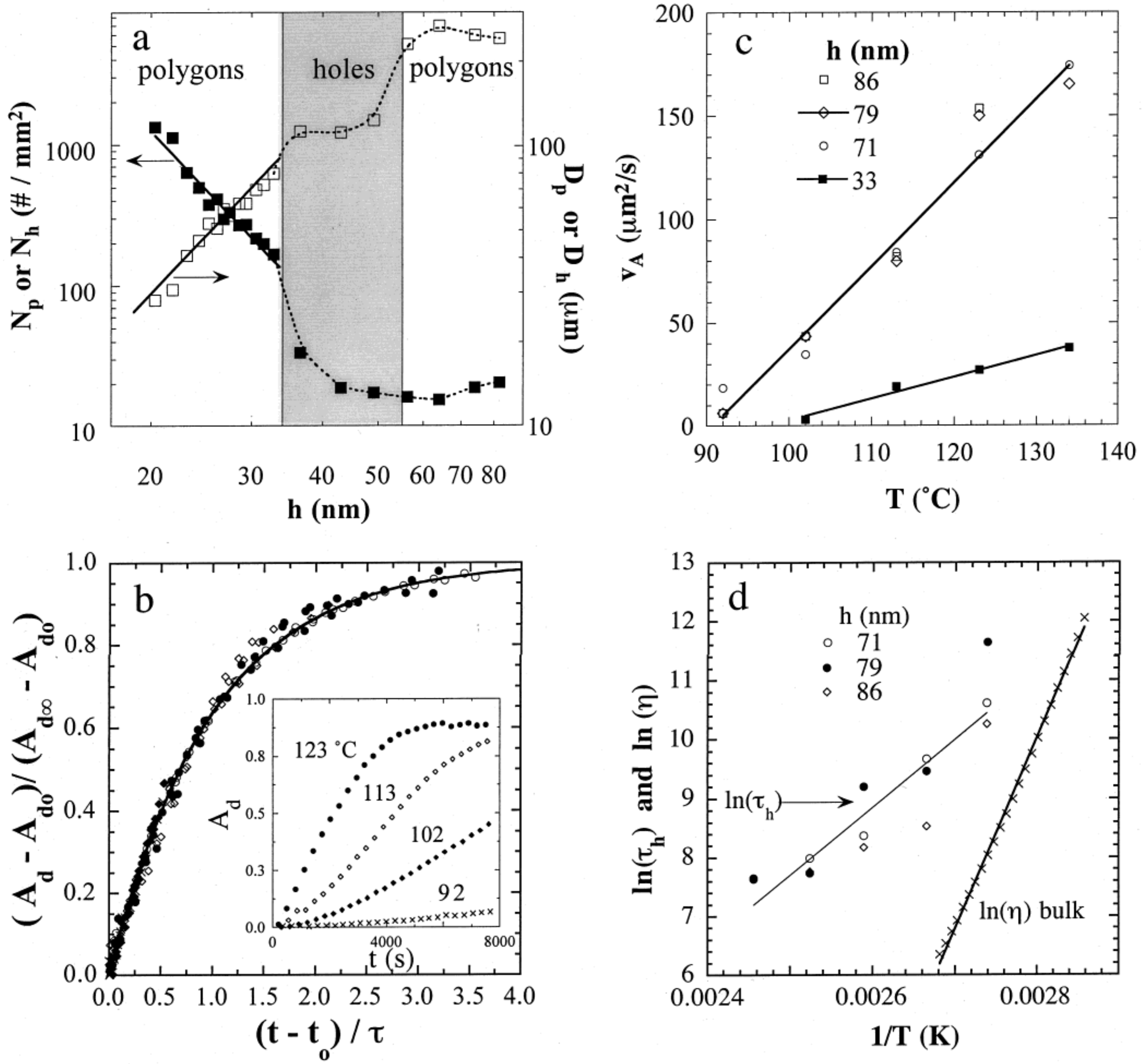

Figure 6. (a) Number of polygons per millimeter squared, N_p, and polygon diameter, D_p (μm), versus thickness at $\bar{T}$ = 124 °C and 20 nm < $\bar{h}$ < 80 nm show scalings characteristic of both heterogeneous and capillary undulation-induced nucleation. (b) $\bar{T}-\bar{h}-t$ superposition of dewet area fraction data onto a universal curve, 92 < $\bar{T}$ < 135 °C, 59 < $\bar{h}$ < 86 nm. Inset: raw dewet area fraction vs time, $\bar{h}$ = 79 nm. (c) Hole area growth velocities, v_A, versus temperature. (d) ln(τ_h) vs 1/$\bar{T}$ (K^{-1}) for τ_h values from fitting procedure for Figure 4b. ln(η) for bulk polystyrene is provided for comparison. The symbol sizes have been adjusted to reflect the standard uncertainty for each measured value in Figure 6.

Table 1. Estimated Values of the Effective Hamaker Constant, *A*, for the Si/SiO$_x$/PS/Air System from Previous Studies Reporting Evidence of Capillary Instability

M_w of PS (g/mol)	A ($\times 10^{-20}$ J)[a]	reference
4000	−7.42	24
28 400	−0.76	31
22 000/39 000	10	23

[a] *A* values are based upon a surface free energy defined as $G(h) = A/(12\pi h^2)$.

onset thickness, h_o, so that the rate of growth of undulations to film rupture competes with other rupture mechanisms (e.g., heterogeneous nucleation). Theory[21,31,32] and experiment[20,22–24,34] indicate that h_o is less than an upper limit of ≈100 nm. For example, experiments on M_w = 4000 g/mol PS at 120 °C indicate $h_o \approx 12$ nm.[24] However, previous experimental studies have not reported precise measurements of h_o or its dependence on molecular mass for polymer films. Once film thickness is below h_o, drainage from heterogeneously nucleated holes competes with growth of capillary undulations as film thinning proceeds, giving rise to the crossover regime. Consider that τ_h, the time constant for drainage of heterogeneously nucleated holes, scales as $\tau_h \sim \eta/h^3$ and that the time constant for growth of the fastest capillary undulation wavelength scales as $\tau_c \sim \eta h^5$.[21,31,32] Hence, as h is decreased below h_o, a critical thickness, h_c, is reached where capillary fluctuations grow faster than heterogeneous dewetting. Only at thicknesses below h_c, where $\tau_c < \tau_h$, will film rupture occur solely by capillary instability, resulting in correlated hole positions.[32,35]

The combinatorial libraries used here encompass a large thickness range, 15 nm < $\bar{h}$ < 90 nm, making it possible to observe both heterogeneous nucleation ($\bar{h} > \bar{h}_o$) and capillary instability nucleation ($\bar{h} < \bar{h}_c$), as well as a crossover regime between the two mechanisms ($\bar{h}_c < \bar{h} < \bar{h}_o$). In Figure 6a, values of N_p and D_p are relatively invariant for $\bar{h}$ > 57 nm (55 ± 4 nm from all five libraries), indicating uniformly distributed nucleation sites expected for heterogeneous nucleation. Since the entire sample was exposed to the same cleaning procedure and airborne particulates, the density of heterogeneously nucleated sites is expected to be uniform across the wafer. Because of the abrupt appearance of correlated undulations on the surface of the unbroken film (Figures 4e,f and 5) below $\bar{h}_o$, we propose that $\bar{h}_o$ = 55 ± 4 nm indicates the onset of capillary instability. We interpret the transition to a scaling regime consistent with capillary instability, e.g., polygon density ($N_p \sim \bar{h}^{-4}$) and diameter ($D_p \sim \bar{h}^2$) in Figure 6a, as indicative that $\bar{h}_c \approx 33$ nm.

We note that voids present in all polymer films prepared in air can also nucleate dewetting in addition to the two forms of nucleation discussed above. Void nucleation was observed in high molecular mass PS films on Si/octadecyltrisilane substrates[30] and was indicated by a scaling of $N_p \sim \exp(-\bar{h})$. This exponential function fits the data in our Figure 6a only slightly less satisfactorily than $N_p \sim \bar{h}^{-4}$. Because of the standard uncertainty in the N_p vs h data, the scaling of N_p or D_p with h is *not sufficient* to distinguish between capillary instability and void nucleation. Void nucleation may occur to some extent in our films; however, there are three reasons why we attribute the dominant nucleation mechanism for $\bar{h}_c$ < 33 nm to capillary instability. First, the transition to N_p vs $\bar{h}^{-4}$ scaling occurs rather abruptly at 33 nm on our libraries. For uniformly distributed bubbles, the void nucleation model does not account for an abrupt change in the N_p vs h dependence. LCIT does provide a physical reason why capillary instability growth rates abruptly overcome growth of heterogeneously nucleated holes below a critical thickness, discussed above. Second, we observe correlated undulations in the early stage of film breakup (Figure 5b), which is not observed or predicted for void nucleation.[30] Finally, we compared the polygon and hole center distributions for $\bar{h}_c$ < 33 nm and $\bar{h}_o$ > 55 nm to check for the presence of correlated nucleation sites, as predicted by LCIT. For $\bar{h}$ < 33 nm, center distributions are correlated as indicated in Figure 7b, which is contrasted with the random hole distribution (Figure 7a) observed for $\bar{h}$ > 55 nm.

The crossover regime 33 nm < $\bar{h}$ < 57 nm corresponds to optical (Figure 4b,e) and AFM images (Figure 5b), indicating an intermediate morphology of both asymmetrical holes and patterned thickness undulations. These early stage surface undulations closely resemble structures observed in previous, noncombinatorial studies reporting capillary instability, particularly those reported by Green et al.[20,24,29] A similar structure involving both heterogeneously nucleated holes and an unbroken spinodal background pattern has been observed for uniform liquid crystal thin films at $\bar{h}$ = 36 nm (Figure 2A of ref 41). The significant difference between dewetting velocities for $\bar{h}$ = 33 nm and $\bar{h}$ = 86, 79, and 71 nm, as shown in Figure 6d, indicates that correlated undulations in film thickness evidently distort and slow the growth process of heterogeneously nucleated holes. This crossover regime between heterogeneous nucleation and capillary instability[32,35] is observed in a straightforward manner with the use of thickness gradient sample libraries.

(a) 79 nm, 85 °C

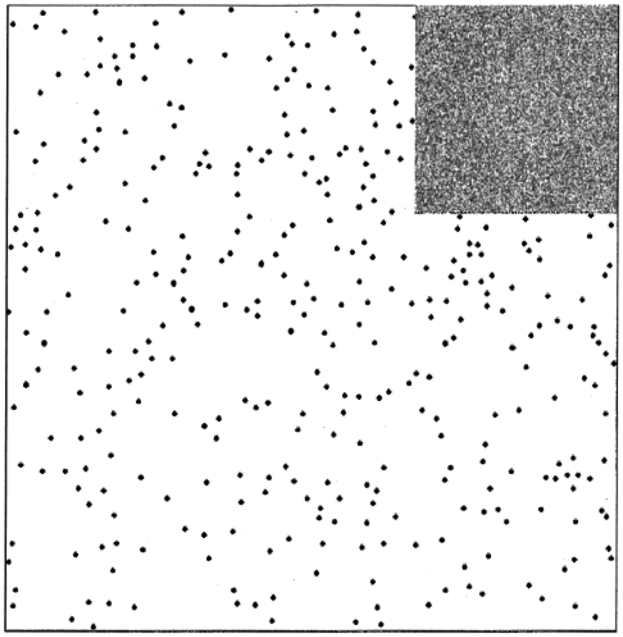

(b) 31 nm, 123 ° C

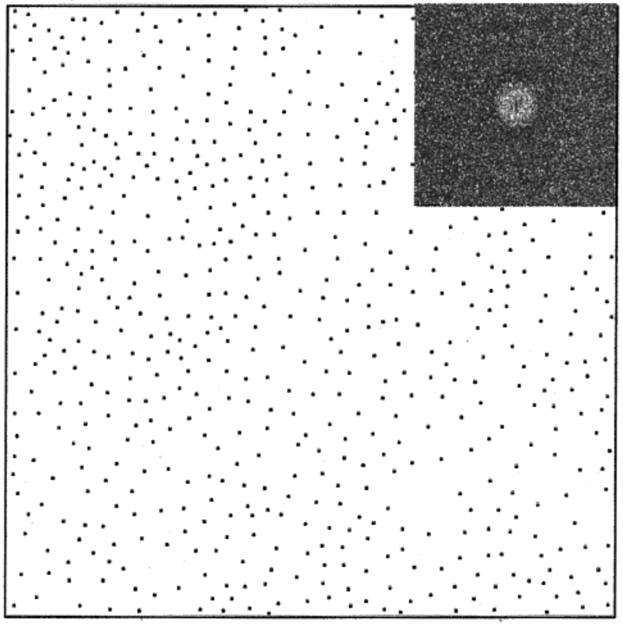

Figure 7. Point set distributions and 2D Fourier transforms (inset) for (a) randomly distributed hole centers at $\bar{h}$ = 79 nm and T = 85 °C, typical of $\bar{h}$ > 55 nm and (b) polygon centers for $\bar{h}$ = 31 nm and T = 123 °C. The image and 2D Fourier transform in (b) show a correlated spacing of nucleation sites expected for capillary instability nucleation, typical of $\bar{h}$ < 33 nm.

For PS with M_r = 1800, we observe the onset of capillary instability at h_o = 55 nm. A previous noncombinatorial study of the Si/SiO$_x$/PS/air system examined four thicknesses, 4.5, 7.5, 12.5, 15, and 35 nm, and reported capillary instability for 12.5 nm and lower sample thicknesses.[24] Because of the small sample set, the precise value of the onset thickness was not located

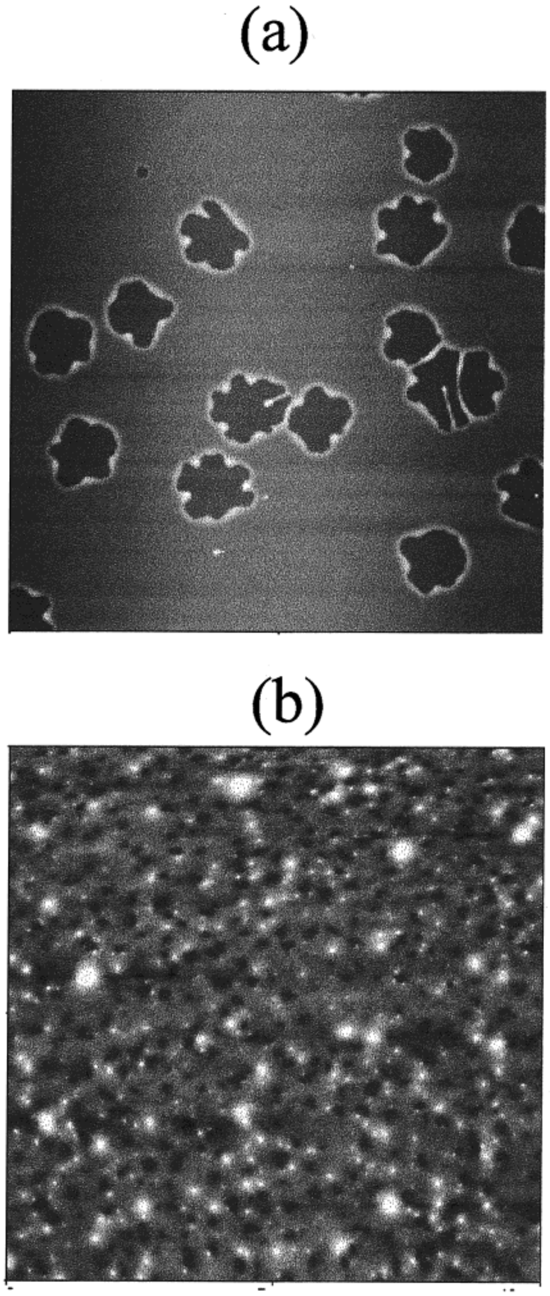

Figure 8. AFM images from a previous study[24] of dewetting on the Si/SiO$_x$/PS/air system using uniform samples. (a) h = 15 nm, t = 12 h, T = 115 °C, image size = 32 μm × 25 μm. Distorted holes are observed, similar to Figure 4b,e of this work. (b) h = 12.5 nm, t = 5.5 h, T = 115 °C, image size = 10 μm × 10 μm. The undulations in surface thickness are similar to those observed in the crossover thickness regime of this work shown in the inset to Figure 5b. We gratefully acknowledge Riu Xie for providing the AFM images.

but is assumed to be between 12.5 and 35 nm. In fact, Figure 8 presents AFM images from this previous study[24] that show a distorted hole morphology and surface undulations similar to that observed here in the crossover thickness regime between heterogeneous and capillary instability nucleation. We suspect that the previous work observed a slightly lower onset thickness primarily because the PS had a higher M_r of 4000. Qualitatively, a higher M_r leads to an increase in viscosity that will require a higher disjoining pressure ($\Pi = A/(6\pi h^3)$), or lower thickness, to induce an observable capillary instability.[32,35] In addition, this previous work used Si wafers from another supplier and slightly different cleaning conditions, which could induce quantitative differences in h_o through modifications in the Hamaker constant. For example, employing a different lot of Si wafers (Polishing Corporation of America) than those used in this paper, we observe the onset of capillary instability at h_o = 65 nm for M_r = 1800. A comprehensive investigation of the factors affecting h_o is beyond the scope of this paper, but we note that it is an ideal topic for a future investigation by the combinatorial approach as we have described in this study.

Interpreting Temperature Dependence. A physical interpretation of the T, h superposition for $\bar{h}$ > 55 nm (Figure 6b) is challenging given the sparsity of work on the temperature dependence of dewetting rates. Brochard-Wyart[21] presents a model of capillary and viscous forces that predicts the isolated hole growth velocity varies as $V \sim \gamma\theta^3/\eta_{\rm film}$, where θ is the equilibrium contact angle and $\eta_{\rm film}$ is the film viscosity. Since $\tau_h \sim 1/V$, then $\tau_h \sim \eta_{\rm film}$ and both τ_h and $\eta_{\rm film}$ should have a similar T dependence. Although measurements of $\eta_{\rm film}$ are not available for our system, measurements of the bulk viscosity, η, of PS used in our study are available. Figure 6d presents a plot of $\ln(\tau_h)$ and $\ln(\eta)$ versus $1/\bar{T}$. Although there is some scatter in the fitted τ_h parameters, the plots indicate a monotonic increase of τ_h with $1/T$. The slopes of lines fitted through the data in Figure 6d can be treated as activation energies,[38] i.e., $\ln(\eta) = a + \Delta\epsilon_\eta/kT$ and $\ln(\tau_h) = b + \Delta\epsilon_\tau/kT$. Since Figure 6d compares thin film (τ_h) and bulk (η) properties, we do not expect the slopes to agree quantitatively. However, $\ln(\tau_h)$ and $\ln(\eta)$ both follow approximately a $1/T$ dependence, and the slopes are of the same order of magnitude. The slopes through the $\ln(\tau_h)$ data do not vary appreciably with thickness and yield an average $\Delta\epsilon_\tau/k$ of 11 800 K, whereas the bulk viscosity data yields $\Delta\epsilon_\eta/k$ = 34 500 K. Discrepancies between these activation energies may reflect differences in the viscosity of bulk and thin-film PS, a subject beyond the scope of this work but discussed elsewhere.[39,40] Tentatively, a smaller activation energy ($\Delta\epsilon_\tau$) for the thin films is consistent with a lower viscosity and glass transition temperature (T_g) than in the bulk, although these values were not measured here. Previous experiments have reported evidence of a decrease in T_g for PS thin films on Si/SiO$_x$ relative to the bulk.[40,42]

Conclusions

By using a novel combinatorial technique to prepare libraries in which the temperature and thickness are varied systematically and continuously, we have measured the temperature−thickness−time dependence of dewetting structures and kinetics. The covered range included thicknesses of 16 < $\bar{h}$ < 90 nm and temperatures of 85 < $\bar{T}$ < 135 °C in two experiments that can be performed in 1 day (although subsequent control experiments were performed also). To validate the approach, the thickness range was chosen to allow observation of dewetting regimes reported in previous noncombinatorial work. Given the known sensitivity of polymer−substrate interactions to even minor differences in cleaning procedures and substrate composition, the quantitative comparisons to previous noncombinatorial work are remarkable. It is evident that the wide range of structures observed on the libraries are a superset encompassing those observed individually in previous work (using uniform samples) over similar thickness ranges.[20,22−24,29,30,34,41] It is important to establish this validation comparison to uniform samples because we have treated the local $\bar{T}$ and $\bar{h}$ values as constants over the image analysis area.

The method presented here is unique in its ability to rapidly identify fundamental trends in film stability, nucleation mechanisms, and dewetting kinetics over a wide range of parameter space. The combinatorial method is a technique that can be used for rapid parametric variation early in a scientific study and to guide parameter selection (e.g., T, h, M_r) for conventional one-sample for one-measurement experiments. In addition, the use of high-throughput measurements covering broad regimes of parameter space may lead to the discovery of novel regions of phase space for thin-film phenomena.[18]

For the Si/SiO$_x$/PS/air system investigated here, three distinct structural regimes were observed on the combinatorial libraries. At thicknesses above $h_o > 55$ nm, holes are nucleated heterogeneously. The appearance of correlated undulations and an intermediate morphology below $\bar{h}_o = 55$ nm is interpreted as the onset of capillary instability. In this crossover regime, 33 nm < $\bar{h}$ < 55 nm, growth of capillary fluctuations competes with heterogeneously nucleated holes. Below $\bar{h}_c$ < 33 nm, nucleation occurs solely by capillary instability. Libraries with continuous thickness variations allow a convenient determination of the location of the heterogeneous to capillary instability kinetic crossover regime. In addition, a superposition of the growth kinetics of nucleated holes for a wide range of T and h values, previously unreported, was observed.

Acknowledgment. We thank Dr. Jack Douglas for his suggestions on the collapse of drainage data to a universal exponential curve. Dr. Mark VanLandingham aided with AFM measurements. Kathy Barnes measured the bulk PS viscosities. J.C.M. was supported by an NRC/NIST Postdoctoral Associateship.

References and Notes

(1) Hanak, J. J. *J. Mater. Sci.* **1970**, *5*, 964.
(2) Dagani, R. *Chem. Eng. News* **2000**, *78*, 66.
(3) Jandeleit, B.; Schaefer, D. J.; Powers, T. S.; Turner, H. W.; Weinberg, W. H. *Angew. Chem., Int. Ed. Engl.* **1999**, *38*, 2494.
(4) Danielson, E.; Golden, J. H.; McFarland, E. W.; Reaves, C. M.; Weinberg, W. H.; Wu, X. D. *Nature* **1997**, *389*, 944.
(5) Danielson, E.; Devenney, M.; Giaquinta, D. M.; Golden, J. H.; Haushalter, R. C.; McFarland, E. W.; Poojary, D. M.; Reaves, C. M.; Wenberg, W. H.; Wu, X. D. *Science* **1998**, *279*, 837.
(6) Sun, X.-D.; Xiang, X.-D. *Appl. Phys. Lett.* **1998**, *72*, 525.
(7) Wang, J.; Yoo, Y.; Gao, C.; Takeuchi, I.; Sun, X.; Chang, H.; Xiang, X.-D.; Schultz, P. G. *Science* **1998**, *279*, 1712.
(8) Briceno, G.; Chang, H.; Sun, X.; Schultz, P. G.; Xiang, X.-D. *Science* **1995**, *270*, 273.
(9) Xiang, X.-D.; Sun, X.; Briceno, G.; Lou, Y.; Wang, K.-A.; Chang, H.; Wallace-Freedman, W. G.; Chen, S.-W.; Schultz, P. G. *Science* **1995**, *268*, 1738.
(10) Reddington, E.; Sapienza, A.; Gurau, B.; Viswanathan, R.; Sarangapani, S.; Smotkin, E.; Mallouk, T. *Science* **1998**, *280*, 1735.
(11) Schmitz, C.; Thelakkat, M.; Schmidt, H. W. *Adv. Mater.* **1999**, *11*, 821.
(12) Klein, J.; Lehmann, C. W.; Schmidt, H.-W.; Maier, W. F. *Angew. Chem., Int. Ed. Engl.* **1998**, *37*, 3369.
(13) Taylor, S. J.; Morken, J. P. *Science* **1998**, *280*, 267.
(14) Bein, T. *Angew. Chem., Int. Ed. Engl.* **1999**, *38*, 323.
(15) Fodor, S. P. A.; Read, J. L.; Pirrung, M. C.; Stryer, L.; Lu, A. T.; Solas, D. *Science* **1991**, *251*, 767.
(16) Dickinson, T. A.; Walt, D. R.; White, J.; Kauer, J. S. *Anal. Chem.* **1997**, *69*, 3413.
(17) Newkome, G. R.; Weis, C. D.; Moorefield, C. N.; Baker, G. R.; Childs, B. J.; Epperson, J. *Angew. Chem., Int. Ed. Engl.* **1998**, *37*, 307.
(18) Meredith, J. C.; Karim, A.; Amis, E. J. *Macromolecules* **2000**, *33*, 5760.
(19) de Gennes, P. G. *Rev. Mod. Phys.* **1985**, *57*, 827.
(20) Reiter, G. *Phys. Rev. Lett.* **1992**, *68*, 75.
(21) Brochard-Wyart, F.; Daillant, J. *Can. J. Phys.* **1990**, *68*, 1084.
(22) Reiter, G. *Langmuir* **1993**, *9*, 1344.
(23) Stange, T. G.; Evans, D. F. *Langmuir* **1997**, *13*, 4459.
(24) Xie, R.; Karim, A.; Douglas, J. F.; Han, C. C.; Weiss, R. A. *Phys. Rev. Lett.* **1998**, *81*, 1251.
(25) *Handbook of Semiconductor Wafer Cleaning Technology*; Kern, W., Ed.; Noyes Publications: Park Ridge, NJ, 1993.
(26) Experimental substrates are coated with a thin layer of oxide and/or organic contaminant. We have attempted to minimize organic contaminants by cleaning our substrates in a piranha bath *immediately* before film coating. In this procedure the wafers are cleaned in a volume fraction 70% H_2SO_4/9% H_2O_2/21% H_2O solution at 80 °C for 1.5 h, which is known to produce an SiO$_x$ layer of thickness $\delta \sim 1-2$ nm. Thus, we refer to our system as Si/SiO$_x$/PS/air. References 28 and 30 discuss the incorporation of thin coatings in calculations of S and A (effective Hamaker constant). When long-range (van der Waals) interactions dominate the early stage of film rupture, S and A are not affected strongly by the thin oxide layer when the film thickness $h \gg \delta$.
(27) Certain equipment and instruments or materials are identified in the paper in order to adequately specify the experimental details. Such identification does not imply recommendation by the National Institute of Standards and Technology, nor does it imply the materials are necessarily the best available for the purpose.
(28) Leal, L. G. *Laminar Flow and Convective Transport Processes*; Butterworth-Heinemann: Boston, 1992.
(29) Masson, J. L.; Green, P. F. *J. Chem. Phys.* **1999**, *112*, 349.
(30) Jacobs, K.; Herminghaus, S.; Mecke, K. R. *Langmuir* **1998**, *14*, 965.
(31) Sharma, A.; Reiter, G. *J. Colloid Interface Sci.* **1996**, *178*, 383.
(32) Vrij, A.; Overbeek, J. T. G. *J. Am. Chem. Soc.* **1968**, *90*, 3074.
(33) Kerle, T.; Yerushalmi-Rozen, R.; Klein, J.; Fetters, L. J. *Europhys. Lett.* **1998**, *44*, 484.
(34) Segalman, R. A.; Green, P. F. *Macromolecules* **1999**, *32*, 801.
(35) Vrij, A. *Discuss. Faraday Soc.* **1966**, *42*, 23.
(36) *Polymer Handbook*, 4th ed.; Brandrup, J., Immergut, E. H., Grulke, E. A., Eds.; John Wiley and Sons: New York, 1999.
(37) Fox, T. G.; Allen, V. R. *J. Chem. Phys.* **1964**, *41*, 344.
(38) Hiemenz, P. C. *Polymer Chemistry*; Marcel Dekker: New York, 1984.
(39) Wallace, W. E.; van Zanten, J. H.; Wu, W. L. *Phys. Rev. E* **1995**, *52*, 52.
(40) Orts, W. J.; van Zanten, J. H.; Wu, W.-L.; Satija, S. K. *Phys. Rev. Lett.* **1993**, *71*, 867.
(41) Herminghaus, S.; Jacobs, K.; Mecke, K.; Bischof, J.; Fery, A.; Ibn-Elhaj, M.; Schlagowski, S. *Science* **1998**, *282*, 916.
(42) Fryer, D. S.; Nealey, P. F.; de Pablo, J. J. *Macromolecules* **2000**, *33*, 6439.

MA001298G